Synthetic β-sheets mimicking fibrillar and oligomeric structures for evaluation of spectral X-ray scattering technique for biomarker quantification

Karthika Suresh[1]*, Eshan Dahal[1] and Aldo Badano[1]

Abstract

Background Archetypical cross-β spines sharpen the boundary between functional and pathological proteins including β-amyloid, tau, α-synuclein and transthyretin are linked to many debilitating human neurodegenerative and non-neurodegenerative amyloidoses. An increased focus on development of pathogenic β-sheet specific fluid and imaging structural biomarkers and conformation-specific monoclonal antibodies in targeted therapies has been recently observed. Identification and quantification of pathogenic oligomers remain challenging for existing neuroimaging modalities.

Results We propose two artificial β-sheets which can mimic the nanoscopic structural characteristics of pathogenic oligomers and fibrils for evaluating the performance of a label free, X-ray based biomarker detection and quantification technique. Highly similar structure with elliptical cross-section and parallel cross-β motif is observed among recombinant α-synuclein fibril, Aβ-42 fibril and artificial β-sheet fibrils. We then use these β-sheet models to assess the performance of spectral small angle X-ray scattering (sSAXS) technique for detecting β-sheet structures. sSAXS showed quantitatively accurate detection of antiparallel, cross-β artificial oligomers from a tissue mimicking environment and significant distinction between different oligomer packing densities such as diffuse and dense packings.

Conclusion The proposed synthetic β-sheet models mimicked the nanoscopic structural characteristics of β-sheets of fibrillar and oligomeric states of Aβ and α-synuclein based on the ATR-FTIR and SAXS data. The tunability of β-sheet proportions and shapes of structural motifs, and the low-cost of these β-sheet models can become useful test materials for evaluating β-sheet or amyloid specific biomarkers in a wide range of neurological diseases. By using the proposed synthetic β-sheet models, our study indicates that the sSAXS has potential to evaluate different stages of β-sheet-enriched structures including oligomers of pathogenic proteins.

Keywords Neurodegenerative diseases, Biomarker, Protein aggregates, β-sheet, Cross-β, Oligomer, Fibril, X-ray scattering

*Correspondence:
Karthika Suresh
karthika.suresh@fda.hhs.gov
[1] Division of Imaging, Diagnostics, and Software Reliability, Office of Science and Engineering Laboratories, Center for Devices and Radiological Health, Food and Drug Administration, Silver Spring, MD 20993, USA

Suresh *et al. Cell & Bioscience*   (2024) 14:26

Page 2 of 18

Introduction

Worldwide, neurodegenerative diseases (NDDs) affect millions and the estimated global number of patients with dementia now exceeds 50 million [1, 2]. These NDDs include Alzheimer's disease (AD), Parkinson's disease (PD), frontotemporal dementia (FTD), prion diseases (PrDs) and amyotrophic lateral sclerosis (ALS). The onset of neurodegeneration is instigated by key events, including protein misfolding, aggregation in the form of oligomers and fibrils and subsequent accumulation in the brain. These processes collectively contribute to the emergence of pathological abnormalities responsible for neurodegenerative disorders.[3, 4]. The proteins incriminated in the accumulation of cerebral misfolded aggregates include amyloid β (Aβ) in AD; tau in AD and FTD; α- synuclein (α- Syn) in PD; prion proteins (PrPs) in PrDs and TAR DNA-binding protein 43 (TDP-43) in ALS [5–9].

The pathogenic fibrillar aggregates of Aβ, tau, α-Syn, PrP and TDP-43 comprise a structural superfamily and share a common substructure at the nanometer length scale, although they do not share sequence homology or related native structure [10]. The characteristic features of these pathogenic aggregates are summarized in Table 1. Aberrant native proteins follow a hierarchical aggregation pathway where the secondary structure of peptides alter its folds from healthy disordered or α-helical to pathological β-sheet enriched structures ranging from soluble toxic oligomers to protofibrils to large fibrillar plaques or tangles. Oligomers are spherical or annular and increase in oligomer size leads to increase in compactness, β-sheet content, structural regularity, stability and hydrophobic surface burial [11]. End-stage, mature, insoluble aggregates take the structural form of thin, unbranched fibrils only a few nanometers in diameter but often micrometers in length. They exhibit a cross-β structural pattern containing ribbon-like β-sheets in which the β-strand segments run perpendicular to the fiber major axis and intermolecular hydrogen bonds of β-strands run parallel to the axis [12]. Generic cross-β structural motif was also reported for pathogenic fibrils of non-NDD amyloidoses as exemplified by amyloid light-chain (AL) amyloidosis, transthyretin (TTR) amyloidosis [13]. In this case, the aggregate depositions can occur across different organs and biological barriers in vivo including spleen, kidneys, liver and heart.

The characteristic tinctorial properties and cross-β diffraction pattern are diagnostic hallmarks of various NDDs [14–16]. Historically, the neuropathological lesions are identified with high certainty by histopathological examination at autopsy. Here, the protein aggregates are selectively stained with histological dyes such as thioflavin-S and Congo red which bind the cross-β structure [14]. Conformation-specific antemortem structural biomarkers are also gaining rapid interest for the detection of different stages of β-sheet-enriched structures [17–20]. In AD, Aβ aggregation into β-sheet-rich structures occur up to 15–20 years prior to clinical manifestation and causes amyloid plaque deposition in the brain. Therefore, research diagnostic criteria in AD recommends amyloid-based biomarkers [21, 22]. The change to an increased β-sheet structure of Aβ aggregates is correlated with cerebrospinal fluid (CSF) AD biomarkers and amyloid positron emission tomography (PET) imaging [15, 17]. The change in secondary structure of Aβ in human blood is also reported as a blood-based amyloid indicator for prodromal AD [16]. Many β-sheet binding ligands including radiolabeled small molecule dyes such as thioflavin and stilbene derivatives have been reported through the development of amyloid PET tracers [23].

Table 1 Summary of reported secondary structures and features of nanoscale structures of various pathogenic proteins in neurodegenerative diseases

Protein	β-Amyloid plaque	α- synuclein Lewy body	Tau tangle	Prion	TDP-43
Disease referring	AD	PD	Down's syndrome	CJD, TSE	FTLD-TDP
Major secondary structure	β-sheet	β-sheet	β-sheet	β-sheet [38]	β-sheet
β-sheet IR absorption wavenumber (cm^{-1})	1632 [39], 1628 [40]	1628, 1680 [41]	1628 [42, 43]	1630, 1628, 1618, 1614 [44]	1626 [45]
% β-sheet	53 [40, 46, 47]	LB core: 49 LB halo: 64 [41]	57 [48]	36–42, 54[a] [49, 50]	52 [51] Wild type: 40 [45]
Conformation, X-ray peak positions (nm)	cross-β, 0.476, 1.06 [52]	cross-β, 0.47, 1 [12, 53]	cross-β, 0.47, 1.3 [48]	cross-β [54], 0.48,1.05[a] [55]	cross-β[b], 0.48, 1.0[c] [56, 57]
Reported filament diameters (nm)	10–20 [58–60]	5–20 [61–63]	8–20 [23]	9–20 [64–67]	15–25 [57, 68, 69]

[a] For scrapie PrP [49], [b]Some studies have also reported that not all TDP-43 aggregates have cross β-sheet structures [70], [c]In-vitro fibrillization, FTLD-TDP: frontotemporal lobar degeneration with TPD-43-immunoreactive pathology, CJD: Creutzfeldt-Jakob disease, TSE: transmissible spongiform encephalopathies

Suresh *et al. Cell & Bioscience*   (2024) 14:26

Page 3 of 18

Additionally, first- and second-generation tau tracers are also based on the detection of specific binding to the β-sheet regions of aggregated tau [24]. The density of binding sites of α-syn and TDP-43 aggregates are lower than Aβ and tau, posing challenge to the development of novel PET tracers for α-syn and TDP-43 [18, 25]. Moreover, chemical and pharmacological properties requirements including blood–brain barrier permeability, high binding affinity and specificity to targets and ability to undergo rapid clearance from normal brain tissue and blood along with high cost and time further add challenges to PET imaging.

Seed amplification assay (SAA) is another reported fluid-based biomarker test of pathology mainly for prion disease and synucleinopathies including PD characterized by protein aggregates [19]. This technique amplifies very small amounts of misfolded aggregates of proteins to the point that can be detected using standard laboratory techniques. A recent CSF-based large cross-sectional study showed that the SAA can classify people with Parkinson's disease with high sensitivity and specificity [20]. This assay is in its developmental stage, and standardization of seed characteristics and aggregation protocol, along with the evaluation of its prognostic value by a longitudinal study, are yet to be established. Non-visualization of regional pathogen distribution adds to its limitations.

Spectral small angle X-ray scattering (sSAXS) is an emerging label-free biomarker quantification tool to detect various β-sheet rich protein aggregates using X-rays [26–31]. This noninvasive technique, comprised of a polychromatic X-ray beam and a spectroscopic photon-counting detector, is shown to capture elastic X-ray scattering signatures of β-sheet structure [26–29]. Preliminary investigations have demonstrated the viability of the sSAXS-based approach in phantoms and mice studies. In contrast to the conventional SAXS, sSAXS allows the imaging of objects as thick as a human head [31]. Brain amyloid burden in AD mice model estimated by sSAXS correlated well with the gold standard histological results [26].

One of the major challenges with the development and optimization of new biomarker quantification techniques for NDDs including sSAXS is the scarcity of human derived pathogenic proteins and high cost of recombinant proteins [32]. Conversions of non-pathogenic peptides and proteins, into aggregates with the characteristics of pathogenic amyloid fibrils have been reported previously [33–37]. Even though, these models qualitatively mimic Aβ-fibrils but often fail to quantitatively match the β-sheet secondary structure. In this present study, we first aim to tune the secondary structure and nanoscopic structures of two protein models to match the % β-sheet content and structures of X-ray scatterers within the length scale of 0.25–45 nm with the NDD related protein aggregates. Mimicking the structures on the farther side of this length scale is beyond the scope of this study. The definition of synthetic aggregates in this study relies on the β-sheet content and X-ray scattering properties within the wavevector range of $q = 0.14$ nm^{-1} to 25 nm^{-1}, corresponding to structural length scales from 0.25 to 45 nm. In this study, the requisite criteria for synthetic fibrils included the ability to form fibrils with elliptical cross-sections, parallel β-sheets, and a cross-β structure with a parallel arrangement of β-sheets with respect to the fibril's major axis. Similarly, the criteria for synthetic oligomers included the presence of a β-sheet secondary structure with a β-sheet content intermediate to that of functional monomers (% β-sheet: 0) and matured fibrils. Additionally, they were required to have antiparallel β-sheets with a high oligomer index (OI > 0.2), an ellipsoidal shape with dimensions comparable to oligomers of NDDs, and an exhibited cross-β X-ray scattering profile.

Here, we engineered the self-assembly of two distinct hydrolyzed globular proteins-bovine serum albumin and β-lactoglobulin to mimic the geometry, secondary structure and β-sheet content of fibrillar and prefibrillar states of Aβ-42. We then assessed the β-sheet detection and quantification performance of sSAXS using these β-sheet mimicking model proteins. Quantitative evaluation of the sSAXS performance under brain tissue environment which mimics the tissue X-ray attenuation characteristics is also performed using two component phantoms. The tunability of β-sheet proportions and shapes of structural motifs, and the low-cost of these β-sheet models can become useful test materials for evaluating β-sheet or amyloid specific biomarkers in a wide range of neurological diseases.

Materials and methods

The recombinant α-synuclein pre-formed fibrils (catalog number- ASF-1001-1) were purchased from rPeptide (Watkinsville, GA). The preformed fibrils were dispersed in buffer solution of pH 7.4 with counter ions of 200 mM tris–HCl, 25 mM NaCl and with 1 wt.% concentration. The Aβ-42 fibrils (SQ-ANAK-80928) were purchased from AnaSpec (Fremont, CA). β-lactoglobulin from bovine milk (lyophilized powder, material number: L3908, genetic A and B mixture, LGAB), bovine serum albumin (material number: A7030, BSA), poly (methyl methacrylate) (average molecular weight 15,000 Da, material number: 200336, PMMA), phosphate buffered saline (pH 7.4, material number: 806552, PBS) and hydrochloric acid (1.0 N solution, material number: H9892, HCl) were purchased from Sigma−Aldrich (St.

Suresh *et al. Cell & Bioscience*   (2024) 14:26

Page 4 of 18

Louis, MO). All chemicals were used as received without further purification.

Preparation of BSA and LGAB solutions and their fibrils

Native proteins were dissolved in distilled water with pH adjusted to 7 and 2. Solvent pH was adjusted to the desired value by adding 1.0 N HCl for pH 2 or PBS buffer for pH 7 and by accurately monitoring using a pH meter (Mettler Toledo, FiveEasy). Protein concentrations were varied from 0.1 (1 mg/ml) to 3 wt.% (30 mg/ml). Protein solutions were stored for 12 h at room temperature prior to any measurements. Fibrils of BSA and LGAB were made by incubating the pH 2 protein solutions in a 90 °C water bath for 12 h followed by rapid quenching of the solution in an ice bath for 1 h. The concentration used for the fibrillization was 3 wt.% (30 mg protein in 1 ml solvent).

Attenuated total reflection Fourier transform infrared (ATR-FTIR) spectroscopy

Secondary structure of heated and unheated protein solutions were studied using ATR-FTIR. A Fourier-transform spectrometer fitted with a diamond attenuated total reflection accessory crystal (Platinum-ATR, Bruker, Germany) and a mercury cadmium telluride detector was used to collect infrared (IR) spectra at room temperature. Coadded 300 scans covering a wavenumber range of $400–4000$ cm^{-1}, were collected using a spectral resolution of 4 cm^{-1} by the OPUS™ software. Approximately ~ 10 µl solutions were pipetted on to the crystal and waited for 10 min to achieve a steady state intensity prior to the measurement. During IR spectra processing, corresponding solvent backgrounds were subtracted along with baseline correction and 13-point smoothing using routines provided by the OPUS software. Proper background subtraction was ensured by zero absorbance in the $1720–1850$ cm^{-1} region.

Peak deconvolution of amide I band ($1600–1700$ cm^{-1}) of proteins were carried out using OriginPro 2021 software (OriginLab Corporation, Northampton, MA, USA). The Gaussian peak-fit model for each spectrum was based on the Fourier self-deconvolution and second derivative analysis (Additional file 1: Figure S1). To distinguish native and fibrils and to compare β-sheet structures between protein solutions, peak fitting was restricted to sub-peak center wavenumber ranges and two peak ratios [Eqs. (1) and (2)]. Designation of wavenumber ranges was based on Table 2.

Prior studies have shown that an antiparallel β-sheet structure is characterized by a low wavenumber, high intensity peak around $1610–1640$ cm^{-1} and a high wavenumber, low intensity band between $1675–1695$ cm^{-1} [71]. Simultaneous presence of both bands is assigned

Table 2 List of vibrational frequency bands in Amide I region of common protein secondary structures in aqueous solution. Information is collected from references [72–74]

Protein secondary structure	Amide I frequency (cm^{-1})
Side chain moieties	1600–1616
Extended chains/β-sheets, aggregated strands	1610–1630
Extended chains/β-sheets/short-segment chains connecting the α-helical segment	1630–1640
Random coil	1637–1648
α-Helix	1648–1660
β-turns	1665–1685
Antiparallel β-Sheets	1675–1695

to oligomers with an antiparallel β-sheet structure, while the presence of only the low wavenumber band ($1610–1640$ cm^{-1}) can be attributed to fibril's parallel β-sheet structure. Therefore, oligomer index [(Eq. 1), where $a_{1675-1695}$ and $a_{1610-1640}$ are area under the peaks present anywhere between 1675 to 1695 cm^{-1} and $1610–1640$ cm^{-1} respectively], will be the most useful criterion for the characterization of oligomers.

$$\text{Oligomer index (OI): } \frac{a_{1675-1695}}{a_{1610-1640}} \quad (1)$$

The total β-sheet content (Eq. 2) in the protein is estimated by taking the ratio of the area under the curve of the peak centered anywhere between $1610–1640$ cm^{-1} ($a_{1610-1640}$) to the area under the curve for the amide I band ($a_{1600-1700}$).

$$\text{β-sheet(\%): } \left[\frac{a_{1610-1640}}{a_{1600-1700}} \right] \times 100 \quad (2)$$

Small- and wide-angle X-ray scattering (SWAXS)

Low energy, monochromatic X-ray scattering experiments were performed using a SAXSpace system (Anton Paar, Graz, Austria) equipped with a copper (Cu) anode, XRD Eigenmann GmbH PW 2273/20 and Mythen microstrip X-ray detector (Dectris Ltd., Baden, Switzerland). The X-ray source was operated at 40 kV and 50 mA and water cooled. The line-focus camera used Cu–Kα radiation with a wavelength, $\lambda = 0.154$ nm (E $= \frac{hc}{l} = 8$ keV) and the irradiation beam was line collimated. A semi-transparent beam stop attenuated the highly intense primary X-ray beam, and the primary beam is used to determine the zero-angle or zero-wavevector (q_0, $q = \frac{4\pi}{\lambda}\sin(\theta)$, where 2θ is the scattering angle) position and to compensate fluctuation in primary beam intensities and sample absorption. Sample to detector

Suresh *et al. Cell & Bioscience* (2024) 14:26

Page 5 of 18

distance was 317 mm and 121 mm for SAXS and WAXS configurations respectively. The scattering vector was calibrated with silver behenate and for current measurements the minimum accessible scattering vector (q_{min}) with SAXS mode was 0.12 nm^{-1}.

For SAXS studies, protein solutions and dispersions were filled in the vacuum-tight, 1 mm quartz capillaries, which were thoroughly cleaned using an alkaline solution (Hellmanex® III, powerful alkaline concentrate) and distilled water. Scattering from corresponding solvent filled capillaries were used as the background during background subtraction. WAXS measurements were conducted on solid proteins packed in a plastic adhesive tape. Solid samples were prepared by drying protein solutions at room temperature. Scattering from adhesive tape was subtracted during background correction. Three separate recordings each with an exposure time of 600 s and 300 s were averaged to obtain final scattering profile for SAXS and WAXS respectively. The total exposure time for SAXS on Aβ-42 fibrils dispersed in pH 7 was 1.5 h due to very low protein concentration. The X-ray exposure time for SAXS on α-synuclein dispersion was 2 h. Three measurements were combined using SAXS analysis software (Anton Paar, Austria, version- 4.20.048).

Scattering patterns were corrected with respect to the primary beam position. The relative intensity of scattering data was further corrected using the transmittance of the direct X-ray beam followed by background subtraction. WAXS data were linearly binned to 100 bins. Slit smeared WAXS data were de-smeared using Lake algorithm [75]. All standard corrections were performed using Anton Paar SAXSanalysis software (Austria, version- 4.20.048).

Spectral small- and wide-angle X-ray scattering (sSAXS)

sSAXS is comprised of high energy, polychromatic X-ray source (tungsten anode, MXR-160/22, COMET), pinhole collimation and spectroscopic photon counting detector (HEXITEC, Quantum Detectors, Oxfordshire, UK). High energy X-rays are used in sSAXS to study thick objects (>3 mm) and the systems allows to fully utilize the available X-ray flux in the choice of energy range without filtering the incident beam. Polychromatic X-rays were generated using 80 kVp tube voltage and 1 mA current and X-ray exposure time of 300 s. X-ray beam was collimated using 2 mm diameter pinhole collimator made of lead. Sample holders were directly adhered on the collimator and the sample to detector distance (SDD) was 350 mm. The space between source to detector was non-vacuumed. Cadmium telluride (CdTe) pixelated detector is 1 mm thick. The detector has 80×80 pixels with 250 µm pixel pitch, where each pixel can measure the energy spectrum. Scattered photons were collected

between 30–80 keV using 27 keV energy threshold, 1 keV energy binning and 300 s X-ray exposure time. The wavevector, q is calculated for each scattering angle (2θ) and energy E using the equation:

$$q(E, \theta) = \frac{4\pi E \sin \theta}{hc} \tag{3}$$

where, hc = 1.24 eV-µm. The charge sharing discrimination (CSD) was applied for charge sharing correction [76]. A beamstop with a 300 µm hole was placed in front of the detector to reduce the spectral degradation from pulse pile-up. Energy dependent transmission factor was calculated by measuring primary beam with and without sample under same experimental conditions. For each measurement, the transmission corrected q data were summed for all energy bins. The final sample scattering profile was obtained after background subtraction. The sample holders were treated as the background. The instrument was calibrated using caffeine powder.

Results and discussion

We first evaluated the secondary structure and % β sheets of recombinant Aβ-42 fibrils, modified and unmodified BSA and LGAB proteins using ATR-FTIR followed by their nanoscopic structure investigations using monochromatic SAXS and WAXS. The selected model protein aggregates which mimic the X-ray scattering characteristics of disease protein aggregates within the length scales of 0.25- to 2-nm were further used for the performance evaluation of sSAXS.

Protein secondary conformations of Aβ-42 fibrils and synthetic oligomers and fibrils

Analysis of amide I band (1700–1600 cm^{-1}) of FTIR is a sensitive and accurate method to address protein secondary structure due to different hydrogen bonding environments within α-helix, β-sheet, turn, or unordered structures. Table 2 summarizes the amide I frequencies of common protein secondary structures in aqueous solution. Additionally, IR spectra can differentiate aggregated protein forms (oligomer vs. fibril) and parallel and antiparallel β-sheet structures within aggregated proteins from native β-sheet protein structures [47, 71, 77]. In our study, fibril with a parallel β-sheet structure and oligomer with an anti-parallel β-sheet structure were distinguished based on the oligomer index (Eq. 1). Prior studies have shown that the oligomer index is above 0.2, typically between 0.2 and 0.3 for proteins with antiparallel β-sheets including Aβ oligomers, but falls below 0.06 for a parallel β-sheet proteins, including Aβ and α-synuclein fibrils [78, 79].

ATR-FTIR study on recombinant Aβ-42 fibrils shows the most abundant secondary structure of Aβ-42, which

Suresh *et al. Cell & Bioscience*   (2024) 14:26

Page 6 of 18

is the parallel β-sheet (55%) with a very small oligomer index (0.01) confirming its fibrillar morphology (Fig. 1a). Prior reports have shown that the fresh wild type peptides exhibit ~48% β-sheet content, and that the fibrils resulting from natural mutations lead to an increase in β-sheet content to ~58%. This increase correlates with greater amyloidogenicity [80]. The β-sheet structure is promoted by the destabilization of α-helices (1660–1648 cm^{-1}) for various systems like Aβ, prion protein (PrP), and the insulin protein [81–83].

To mimic the fibrillar morphology and β-sheet content of A β-42 on commercially available globular proteins, we solution-processed two different and unrelated proteins, LGAB and BSA, at different pH and thermal conditions. The selection criteria for proteins to prepare synthetic aggregates involved identifying those capable of modifying their conformation and nanoscopic structures through physical modifications such as thermal treatments and by tuning electrostatic interactions. Partial unfolding of the protein is considered to precede

aggregation and a distinct feature of protein aggregation is the increase of β-sheet structures. The extent of net charge on the polypeptide chain can govern the intermolecular interactions and the final aggregated structure. Therefore, the unfolding of these globular proteins is a complex process that is pH dependent due to its effects on zeta potential starting in a noncooperative transition above 30 °C. The isoelectric point (IEP) of BSA and LGAB lies between pH 4.7 to pH 5.1. The zeta potential increased from ~ − 30 to ~ 30 mV with a decrease in pH from 7.0 to 2.0 (Additional file 1: Figure S2). Previous studies have reported an expanded conformation of BSA at pH 2, and a monomer to dimer transition for LGAB below pH 2.5 that is accompanied by increases in volume and adiabatic compressibility [84, 85]. Therefore, our study limits to two pH values: 2 and 7 (neutral).

β-lactoglobulin is a predominantly β-sheet protein with more than 50% β-sheet content even in the as received powder state without any modifications (Fig. 1b). At pH 2 and room temperature, the increase in LGAB
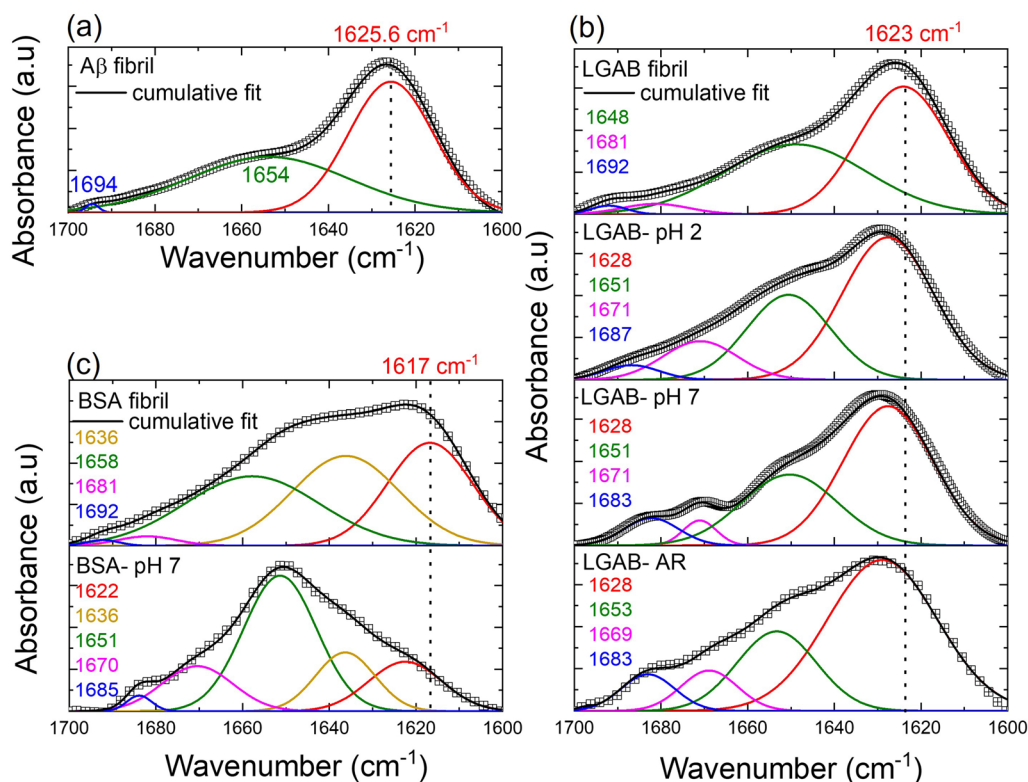

Fig. 1 ATR-FTIR spectra in the amide I region (1700–1600 cm^{-1}) of (**a**) amyloid fibrils (Aβ-42) formed in vitro (**b**) LGAB as received in the powder form (LGAB-AR), LGAB-AR dissolved in pH 2 and 7 (LGAB-pH2 and LGAB-pH7 respectively) and LGAB treated at pH 2 at 90 °C for 12 h (LGAB fibril) and (**c**) BSA heated at 90 °C for 12 h in pH 2 solution (BSA-fibril) and as received (BSA-AR). Raw data are plotted using symbols. Each spectrum was decomposed by fitting with Gaussian curves. The peak centers (in cm^{-1}) of each decomposed peak are indicated in each figure, using the color corresponding to the respective peak color. The identification of protein secondary structure for each wavenumber can be determined based on Table 2. The sum of the fitted curves is displayed as a black continuous line for each. The dotted lines are shown at low wavenumber to facilitate the identification of the major difference between spectra in the β-sheet region. Change in oligomer index with protein modifications can be observed from the change in the area under the curves of blue curves at high wavenumber

Suresh *et al. Cell & Bioscience*   (2024) 14:26

Page 7 of 18

concentration from 0.1 to 3 wt.% shows a change in the shape of amide I band (Additional file 1: Figure S3). vandenAkker et al. have shown that the low concentration peptides (3–4 wt.%) are optimum for the higher persistence length, long and straight fibrils in contrast to higher concentrations (4–7.5 wt.%) [86]. The negative correlation between monomer concentration in one end and β-sheet content, fibril length and persistence length on the other end can lead to more nuclei and shorter worm-like aggregates at high concentrations. Hence, in this study, the protein concentration for fibrillization at pH 2 and 90 °C for 12 h was limited at 3 wt.%. Deconvolution of amide I spectra of 3 wt.% LGAB indicates the percentage of β-sheet is between 50–60% and does not show any specific trend with pH change or with increase in processing temperature (Table 3). However, at room temperature, the oligomer index decreased when pH reduced to 2 (OI = 0.06) compared to neutral pH (OI = 0.12), even though the low wavenumber β-sheet peak position was at 1628 cm^{-1} in both cases.

However, heating of LGAB solution at pH 2 to 90 °C for 12 h lead to a shift in the β-sheet peak position to a lower wavenumber (approximately 1624 cm^{-1}) along with an OI of 0. 02. The different position of the amide I maxima suggests difference in the structure. It has been previously shown that such red-shifting of this β-sheet band in FTIR spectra is due to the presence of intermolecular rather than intramolecular β-sheet structure [87]. This trend is often observed in the spectra of amyloid fibrils relative to the spectra observed for their constituent natively folded proteins. The decrease in OI due to oligomer loss by the reorganization of β-strands from an antiparallel to a parallel β-sheet supports the prediction of LGAB fibrillization. Interestingly, the features of LGAB fibrillization were absent in LGAB-pH 2 solution heated at 45 °C for 13 days (Additional file 1: Figure S4),

confirming the requirements of more cooperative transitions for protein fibrillization.

In contrast to LGAB, the unmodified BSA protein is majorly α-helical in nature (50% α-helix and 18% β-sheet), as supported by previous reports [88, 89]. Heating it to 90 °C in pH 2 buffer led to change in IR spectra shape (Fig. 1c). To summarize, there was a clear decrease in α-helical (from 50 to 34%) and β-turn (from 16 to 2%) contents and an increase in β-sheet (from 18 to 33%) and random coil (from 17 to 30%) with a drastic reduction in OI to 0.06. Increase in average molecular size with decrease in pH below the isoelectric point (pH 4.7) and no significant change in dimensions between neutral and IEP were reported previously [84]. This is due to the unfolding of BSA below the IEP. The increased β-sheet content at pH 2 and 90 °C could be due to BSA aggregation and thus the fibril formation. However, compared to BSA fibrils, % β-sheet and OI of LGAB fibrils better match with the recombinant Aβ-42 fibrils.

Solution small angle X-ray scattering of Aβ-42 fibrils and synthetic oligomers and fibrils

To study the overall structure of proteins and their structural perturbations upon environmental modifications by change in pH and temperature, SAXS (3.2–44.4 nm) and WAXS (0.34–2.1 nm) methods were used. Global alterations in proteins are reflected in the radius of gyration (R_g), pair distance distribution ($p(r)$) and appearance of Kratky plots. Small-angle scattering (X-ray and neutron) and X-ray fiber diffraction (XRD) studies have been reported for brain derived, recombinant and synthetic amyloid or amyloid-like peptides in the presence of solvents [90–92]. We used SAXS to provide information on the fibril cross-section dimension and shape for recombinant Aβ-42 fibrils dispersed in aqueous phosphate buffer at pH = 7 at room temperature.

Table 3 Summary of parameters extracted by analyzing ATR-FTIR and solution SAXS spectra of α-synuclein fibril, Aβ-42 fibril and modified and un-modified protein solutions of LGAB and BSA

Sample	Vibrational frequency peak center of β-sheet/ aggregated structure (cm^{-1})	% β-sheet	Particle shape	R_g(nm)	a (nm)	b (nm)
α- synuclein fibril- pH 7.4	1630	51 ± 2	Elliptical cylinder		3.5 ± 0.05	13.3 ± 0.2
Aβ-42 fibril-pH 7	1626	55 ± 2	Elliptical cylinder		3.0 ± 0.08	9.2 ± 0.1
LGAB fibril-pH 2	1624	54 ± 3	Elliptical cylinder		1.1 ± 0.03	9.8 ± 0.09
BSA fibril-pH 2	1617	33 ± 5	Elliptical cylinder		1.4 ± 0.2	10.4 ± 0.4
LGAB-pH 2	1628	54 ± 2	Prolate ellipsoid	2.3 ± 0.05	1.5 ± 0.01	3.2 ± 0.02
LGAB-pH 7	1628	55 ± 4	Prolate ellipsoid	2.2 ± 0.01	1.3 ± 0.05	3.3 ± 0.04
BSA-pH 2	1622	20 ± 3	Prolate ellipsoid	3.0 ± 0.02	1.3 ± 0.02	4.6 ± 0.02
BSA-pH 7	1622	18 ± 2	Prolate ellipsoid	2.9 ± 0.01	1.4 ± 0.01	4.5 ± 0.02

Averaged values ± standard deviations are from three independent measurements on fresh samples

The 1D scattering profile of Aβ-42 fibrils exhibits classic q^{-1} scaling in the low q region characteristic of scattering from a one-dimensional object. The fibrils are modeled as elliptical cylinders. In general, SAXS measures the product of form ($P(q)$) and structure ($S(q)$) factors ($I(q) \propto P(q)S(q)$). In our model, protein–protein interactions are neglected due to low protein concentration and strong charge screening of the added buffer solvent. Based on prior reports, the fibrils are very long ($L \gg q_{min}^{-1}$) and this length cannot be measured with the accessible experimental q_{min}-value. Based on the studies by Quillin and Matthews [93] and Lattanzi et al. [90], the form factor was factorized into a product of cross-section and cylinder over-all length contributions. The elliptical cylinder cross-section form factor ($P_c(q)$) was written as:

$$P_c(q) = \frac{2}{\pi} \int_0^{\pi/2} \left(\frac{2J_1(ql)}{ql} \right)^2 d\varphi \tag{4}$$

where

$$l = \left((a \sin \varphi)^2 + (b \cos \varphi)^2 \right)^{1/2} \tag{5}$$

$J_1(ql)$ is the first order Bessel function of ql, a, and b are minor and major semiaxes and φ is the polar angle.

The solid line (Fig. 2a) is the modeled scattering profile and $a = 3$ nm and $b = 9.2$ nm described the SAXS pattern well. The values match well with the prior reports based on SAXS and atomic force microscopy (AFM) on mature Aβ-42 fibrils (Table 1). The slight deviation at lower q-values could be most likely due to the fibril-fibril attractive interactions arising from hydrophobic interactions. Similar observations were reported for Aβ-42 and α-synuclein [90, 94]. Protein conformational changes and aggregation can be readily assessed from the pair distance distribution function ($p(r)$). This represents the distribution of distances between volume elements inside the particle weighted by the excess density distribution. $p(r)$ was calculated from scattering intensity ($I(q)$) using the indirect Fourier transform method:

$$I(q) = 4\pi \int_0^{D_{max}} p(r) \frac{\sin(qr)}{qr} dr \tag{6}$$

D_{max} is the maximum diameter of the particle. The $p(r)$ of Aβ-42 fibril exhibited a skewed distribution, corroborating the notion of a long rod with a clear maximum at $r \sim 4.5$ nm corresponding to the radius of the cross section. The information on D_{max} for rods is limited by the number of Shannon channels (N_s), where
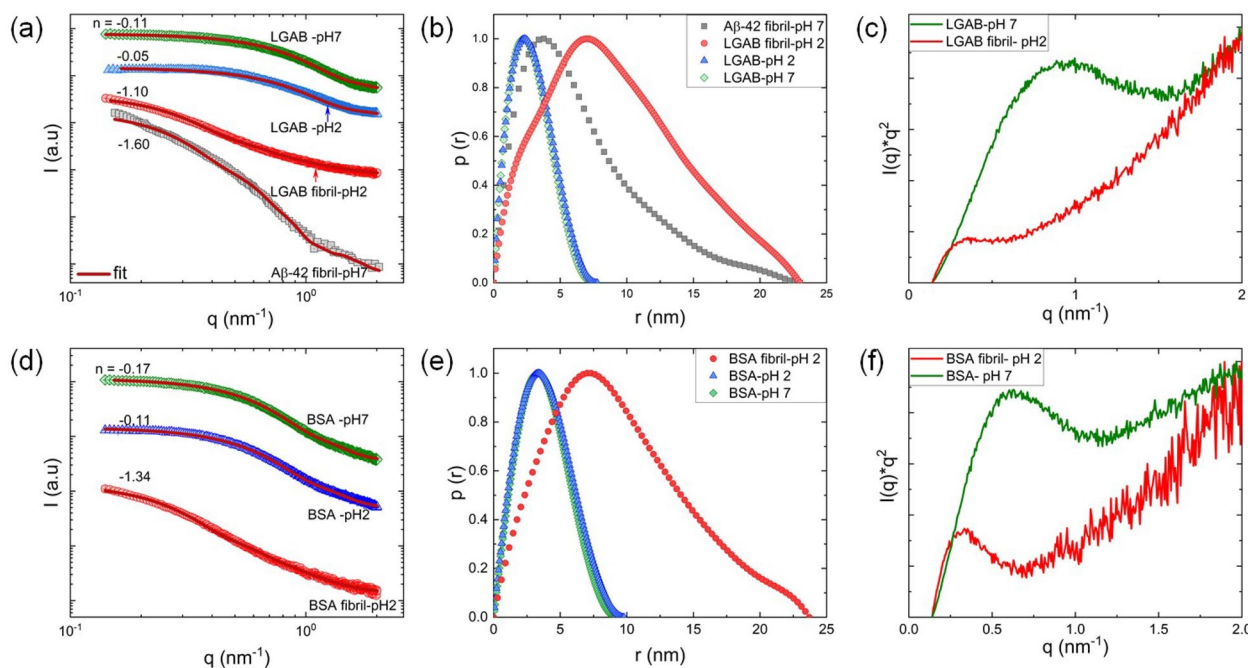

Fig. 2 Comparison of structures of Aβ-42 fibrils, modified and unmodified LGAB and BSA using solution SAXS. **a**, **d** 1D scattering profiles where the solid lines are calculated scattering profiles where fibrils are modeled as elliptical cylinders and proteins dissolved in pH 2 and 7 are modeled as ellipsoids. The Y-axis of the curves are scaled for better visualization. **b**, **e** Normalized pair distance distribution ($p(r)$) functions calculated from inverse Fourier transforms of 1D scattering profiles without model predictions. **c**, **f** Kratky plots of LGAB and BSA fibrils compared with their proteins dissolved at pH 7 prior to modifications

Suresh *et al. Cell & Bioscience*   (2024) 14:26

Page 9 of 18

$N_s = D_{max}(q_{max} - q_{min})/\pi$ [95, 96]. In our study for fibrils, we forced $p(r)$ to converge to zero at experimentally accessible q_{min}. Therefore, $p(r)$ and continuum model fitting reveal an elliptical cross-section for Aβ-42 fibrils.

The scattering intensity of unheated solutions of LGAB and BSA in pH 2 and 7 followed the asymptotic slope ~ 0 at low q region ($q < 0.3$ nm^{-1}, Fig. 2a, d). The almost symmetrical shape of $p(r)$ of native proteins resembles the $p(r)$ of sphere (Fig. 2b, e). However, on close inspection, the asymmetry at large r values can be seen, indicating very slight elongation of the spherical species. Therefore, the 1D scattering data of untreated proteins were modelled as prolate ellipsoid and fit parameters are reported in Table 3. The axial ratio (b/a) of BSA ellipsoids are slightly higher than LGAB ellipsoids. The radius of gyration (R_g), the most common descriptor to quantify the overall size of proteins in solution, was determined based on the whole q-range of the scattering curve through $p(r)$ as well as using the classical Guinier approximation ($qR_g < 1.3$).

$$R_g^2 = \frac{1}{2} \int_0^{D_{max}} r^2 dr \tag{7}$$

$$I(q) \approx I(0)e^{-q^2 R_g^2/3} \tag{8}$$

The close agreement between real space R_g (from $p(r)$) and reciprocal space R_g (from Guinier region) indicates the absence of big aggregates in unheated protein solutions. Kratky representation was used to easily identify the protein structural compaction. At pH 7, both BSA and LGAB didn't exhibit a perfect bell shape, instead showing a less compact, partially unfolded profile (Fig. 2e, f).

Prolonged heating of LGAB and BSA at 90 °C and pH 2 led to an increase in the scattering intensity slope to ~ -1 at low q region (Fig. 2a, d). This reveals the presence of a rod-like structure and confirms protein fibrillization under this condition. The skew shaped $p(r)$ distribution also supports this observation (Fig. 2b, e). The 1D scattering profiles were modeled similarly to the Aβ-42 fibril using the elliptical cylinder cross-section form factor ($P_c(q)$). The model fits matched quite well with the experimental data (Fig. 2a,d). The major and minor semi-axes length scales of LGAB and BSA fibrils are similar to matured Aβ-42 fibril (Table 3). Kratky plots show that thermal treatment decreases the protein compaction, and LGAB exhibited complete unfolding (Fig. 2e, f). However, heated BSA dispersion exhibited a prototypical feature of globular and disordered domains in the partially unfolded construct (Fig. 2f). This could arise from the mixture of fibril and oligomeric states, even though the

system is dominated by the fibrillar form as confirmed by $I(q) \sim q^{-1.34}$ (Fig. 2d). Therefore, the fibrillization kinetics are faster for LGAB compared to BSA under similar environmental conditions. Our ATR-FTIR study and solution SAXS confirm that the unmodified LGAB and BSA are primarily ellipsoids ($I(q) \sim q^0$). The dominant aggregate form of model proteins modified at 90 °C and pH 2 is fibrils ($I(q) \sim q^{\sim -1}$). Therefore, we did not further purify the system to discern subpopulations as this may better represent the complexity involved in diseased human brain tissue.

Cross-β sheet structure of Aβ-42 fibrils and synthetic oligomers and fibrils

We also collected data on WAXS to clarify whether the modified fibrils have amyloid characteristics as the gold standard for detecting cross-β structures. The principal features of the WAXS profiles of non-oriented fibrils of Aβ-42, LGAB and BSA consist of broad intense peaks at around $q = 6.3 nm^{-1}$ and $13.1 nm^{-1}$, corresponding to Bragg spacings of $d = (2\pi/q) = 1.0$ nm and 0.47 nm respectively (Fig. 3a). These peaks are consistent with the reported spherically averaged cross-β pattern of matured amyloid fibrils (Table 1). The peak at 13.1 nm^{-1} arises from the hydrogen-bonded stacking of β-strands perpendicular to the fiber axis, whereas the 6.3 nm^{-1} peak arises from adjoining β-sheets that run the length of the fibers that are held together by zipper-like side chain interactions between the β-sheets [97]. Interestingly, a qualitatively similar WAXS pattern is observed for unmodified BSA and LGAB spheroids. High q scattering profiles obtained from sSAXS using polychromatic X-ray beam also support these observations. The β-strand separation of 0.47 nm ($q = 13.1$ nm^{-1}) is a characteristic feature of parallel and antiparallel β-sheets in folded monomeric proteins as well as in β-sheet aggregates of short peptides. The characteristic distance of 1.0 nm is also observed for these spheroids similar to pattern that arises from the presence of parallel, mature amyloid fibrils (Fig. 3b). FTIR and SAXS studies revealed an antiparallel, prolate ellipsoid structure for unmodified proteins (Figs. 1 and 2). Therefore, the peak at q = 6.3 nm^{-1} is not arising from the presence of mature amyloid-like fibers. More recently, X-ray microdiffraction and solid-state nuclear magnetic resonance studies have demonstrated that soluble, globular, high molecular weight oligomers can adopt either a cross-β conformation containing parallel or an anti-parallel β-sheet arrangement while still being in a globular shape. Stroud et al. have shown that antiparallel Aβ-42 prefibrillar oligomers, with around 30% β-sheet content and the size 13–28 nm in the longest direction, have diffraction pattern similar to those arising from the presence of parallel, mature amyloid fibers [98]. Here,
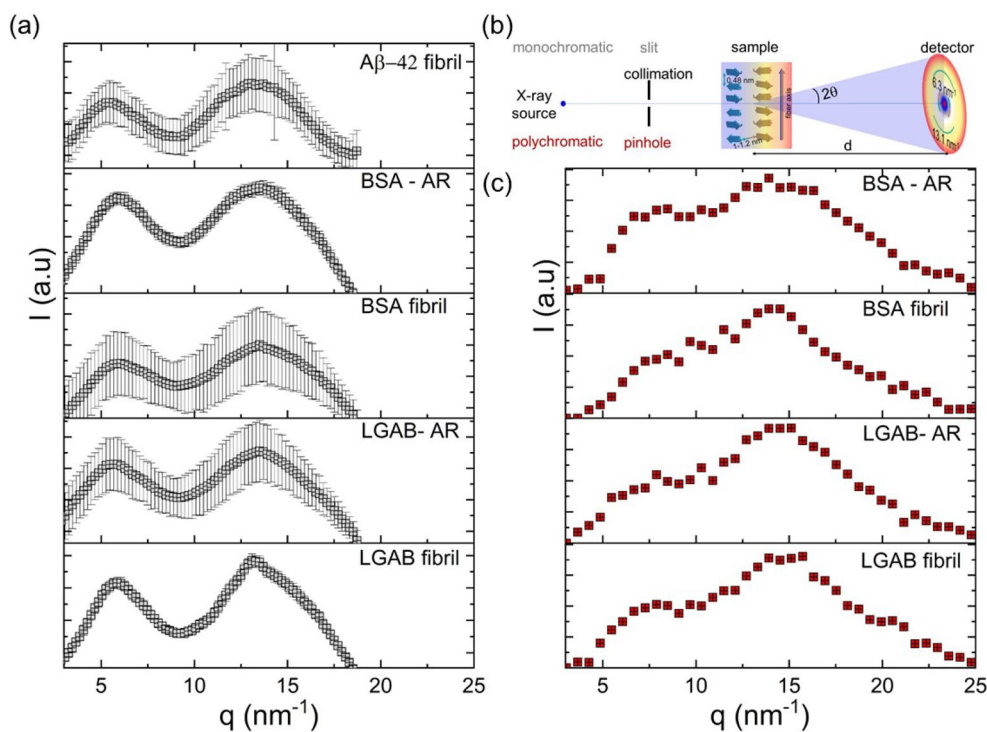
Fig. 3 High q (> 3 nm^{-1}) scattering profiles of Aβ-42 fibrils, modified and unmodified LGAB and BSA in the powder or flake forms measured from **a** monochromatic, low energy wide angle-X-ray scattering and **c** sSAXS. **b** The differences in the experimental set-ups of monochromatic WAXS and sSAXS are shown in the schematic. sSAXS covers the length scales of 0.25- 2.1 nm. All samples exhibit characteristics of cross-β motifs with reflections ~q= 6.3 and 13.1 nm^{-1}

the cross-β structure for fibrils or oligomers are made of adjacent β-sheets that adhere to each other through interpenetration of protein side chains. Gu et.al. have reported similar observations for Aβ-42 oligomers prepared using a fusion protein [99]. We believe the 1.0 nm and 0.47 nm reflections could be arising from the 18 and 55% antiparallel β-sheets present in BSA and LGAB spheroids respectively. Therefore, our study also suggests that the unmodified spheroids can serve as the β-sheet structure mimicking model proteins for amyloid-like oligomers. The detectability of oligomer models using sSAXS is quite promising as an early amyloid detection approach for neurodegenerative diseases. Our study demonstrated the capability of sSAXS to detect up to 18% β-sheet.

Comparing Aβ-42 fibrils and model aggregates with α-synuclein aggregates

The wide-angle X-ray scattering of α-synuclein fibrils under neutral pH conditions revealed a distinctive cross-β structure, evidenced by peaks centered at $q = 6.7$ nm^{-1} and 13.1 nm^{-1}. These peaks correspond to the spacings between inter β-sheets and inter β-strands, respectively (Fig. 4b). Furthermore, the arrangement of β-strands is observed to be perpendicular to the fibrillar axis. We determined the cross-sectional dimensions of the fibrils by modeling them as elliptical cylinders using an Eq. 4. An elliptical cross-section with a minor axis of $a = 3.5$ nm and major axis of $b = 13.3$ nm, effectively describes the scattering pattern, as depicted in the fit in Fig. 4c. The radius of gyration (R_g) of α-synuclein, purified from human red blood cells, is reported to be 3.3 ± 0.3 nm [101]. This value is nearly double the theoretically estimated R_g for a folded globular protein with 140 amino acid residues, based on the equation $R_{g,theory} = 0.29n^{1/3}$, where n is the number of amino acid residues, and smaller than that of a random coil with a similar molar mass (~5 nm). This suggests that the 3 nm size of α-synuclein could arise from the partially folded intermediate state of the protein chain. The fibril length was not measurable in this experiment because the overall length exceeded the experimentally accessible minimum q range (L > $\frac{1}{q_{min}}$). The shape of pair distance distribution function $p(r)$, which is peaked around 3.65 nm, further confirming the long cylindrical morphology of the fibrils (Fig. 4d). The estimation of the maximum pair distance is beyond the detection limit of the current experimental setup; hence, the $p(r)$ is forced to zero at the maximum accessible q_{min}.
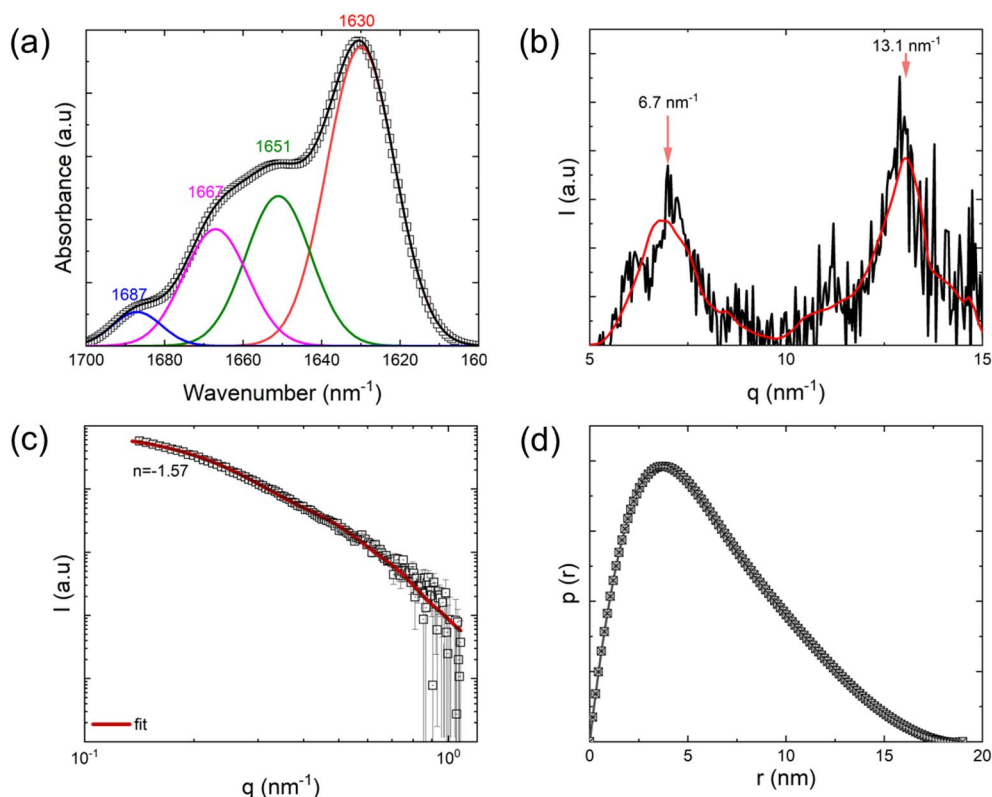
Fig. 4 The secondary structure and X-ray scattering properties of recombinant α-synuclein fibrils dispersed in a buffer solution at a concentration of 1 wt.%. **a** The amide I region of the ATR-FTIR spectrum is analyzed, and the secondary structures in this region are deconvoluted using peak analysis. **b** The WAXS profile of 1 wt.% α-synuclein fibrils, dispersed in the buffer solution and exposed to X-rays for a total of 2 h. The denoised spectrum is depicted by the red curve, obtained through wavelet denoising as described in the reference [100]. **c** The 1D SAXS profile of the 1 wt.% α-synuclein fibrillar dispersion. The fibrils are modeled as elliptical cylinders with delta distribution, and the calculated model scattering curve is displayed as the fit. **d** The pair distance distribution function, p(r), of α-synuclein fibrils is illustrated

In conclusion, our FTIR, WAXS, and SAXS studies suggest that the secondary structure and nanostructure of α-synuclein fibrils are comparable to Aβ-42 fibrils. Furthermore, the model LGAB fibril mimics the β-sheet content, oligomer index, and X-ray scattering characteristics of both Aβ-42 and α-synuclein fibrils. Additionally, the synthetic fibrils needed to be quantitatively comparable to protein aggregates associated with neurodegenerative diseases in terms of β-sheet content, oligomer index, and cross-sectional dimensions. The structural characteristics of LGAB fibrils, formed by thermally modifying a 3 wt.% (in mg/ml) aqueous solution of native protein adjusted to pH 2 at 90 °C for 12 h, were both qualitatively and quantitatively comparable with recombinant amyloid β-42 fibrils and α-synuclein fibrils.

Performance evaluation of sSAXS using synthetic oligomers

We additionally evaluated the performance of sSAXS to detect and quantify oligomers in various conditions. These conditions include varying oligomer fractions in tissue-mimicking environment, target oligomer global densities and different packing densities of the deposits. We first evaluated the potential of sSAXS on accurate detection and quantification of different % of β-sheet oligomers from tissue equivalent environment. For this, we selected oligomer-like, unmodified BSA (BSA-AR, β sheet (%): 18) and LGAB (LGAB-AR, β sheet (%): 55). We prepared mixtures by blending protein with different proportions of polymethyl methacrylate (PMMA) powder. Prior studies have shown PMMA as human tissue equivalent material in terms of X-ray attenuation properties [102, 103]. Additional file 1: Table S1 shows similar X-ray mass attenuation coefficients (μ_m, Additional file 1: Eq. S1) of PMMA and brain tissue (white matter and grey matter) in the 30–80 keV energy range. However, we have not compared the X-ray scattering profiles of PMMA and brain tissue.

In this study, the protein mass fraction ($f_{protein}$) was varied from 0 to 1. Uniform packing density across blends was ensured by applying a fixed compression stress (Additional file 1: Figure S5). The sSAXS profile of

PMMA powder shows a broad peak between $q \sim 3$ nm^{-1} and ~ 25 nm^{-1}. Second derivative and Fourier self-deconvolution analyses resolve two overlapped peaks in the scattering spectra. The centers of deconvoluted individual peaks were at $q = 9$ nm^{-1} and 13.1 nm^{-1} (Fig. 5c). The incorporation of an artificial peak center at $q = 6.3$ nm^{-1} shows the absence of a peak at 6.3 nm^{-1} for PMMA. The

deconvoluted sSAXS spectra of PMMA- oligomer blends (PMMA/BSA and PMMA/LGAB) showed three peaks with peak centers at $q = 6.3$ nm^{-1}, 9 nm^{-1} and 13.1 nm^{-1} (Fig. 5b, e, Additional file 1: Figure S6). The 6.3 nm^{-1} peak solely arises from oligomer β sheet as observed in Fig. 5a and d. The 13.1 nm^{-1} peak is contributed by both β sheet and PMMA. Therefore, the quantification of
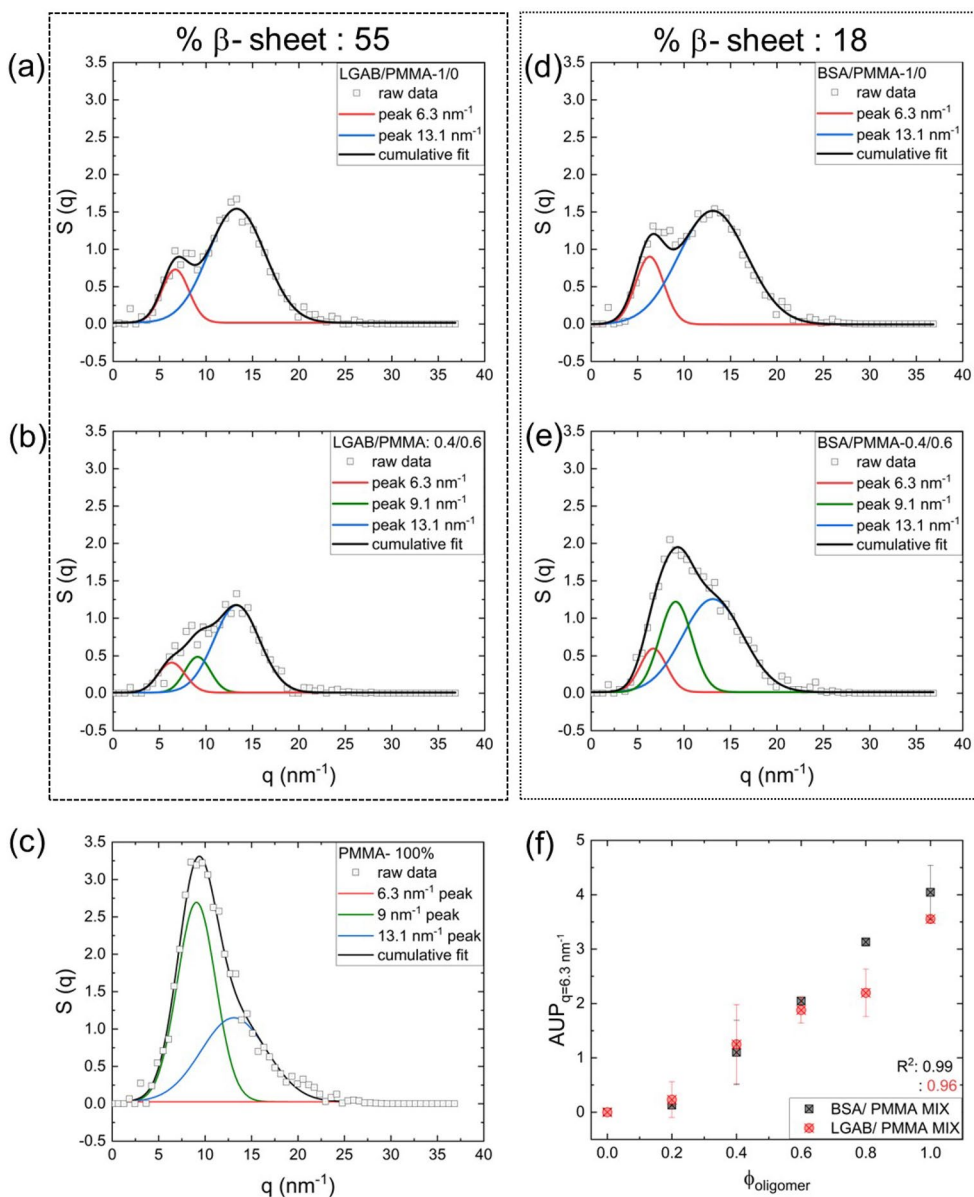

Fig. 5 sSAXS calibration using amyloid-like oligomers of LGAB and BSA with % β-sheets of 55 and 18 respectively. sSAXS spectra of unmodified **a** LGAB and **d** BSA oligomer and **b**, **e** their 0.4/0.6 (40% oligomer and 60% PMMA) blends with tissue mimicking polymethyl methacrylate (PMMA). **c** sSAXS spectrum of pure PMMA powder. Spectra of oligomers and PMMA are deconvolved using Gaussian curves. Raw data are shown with symbols and the cumulative fits are shown with black lines. In (**c**) for pure PMMA, a peak center at $q = 6.3$ nm^{-1} is deliberately inserted during deconvolution and the resultant curve indicates the absence of corresponding peak in the raw data. **f** Area under the peak of $q = 6.3$ nm^{-1} ($AUP_{q=6.3nm^{-1}}$) as a function of oligomer weight fraction ($f_{oligomer}$) for BSA and LGAB. For each oligomer weight fraction, three independent measurements were performed on freshly prepared samples and the error bars in (**f**) are estimated based on that

β sheet in the oligomer/PMMA mix was based on the area under the peak (AUP) of 6.3 nm^{-1} ($AUP_{q=6.3\,nm^{-1}}$). $AUP_{q=6.3\,nm^{-1}}$ of PMMA blend with BSA or LGAB showed a linear correlation with the protein mass fraction (Fig. 5f). As expected, the $AUP_{q=13.1\,nm^{-1}}$ were almost independent of $f_{oligomer}$. We believe slight heterogeneity within the PMMA/LGAB blend due to fluffy texture of LGAB powder decreased the R^2 value compared to the BSA/PMMA mix. Most importantly, high R^2 values (>0.95) validate the potential of sSAXS for accurate β-sheet quantification, even from oligomer-like proteins.

We further validated the sSAXS performance at different target volumes by varying the target thickness (Fig. 6a, b). In this study, we used BSA-AR oligomer as the target due to its lowest β-sheet content (18%) among all samples studied here. The polychromatic pencil beam was geometrically focused on a region of interest. Samples were directly placed on a 2 mm pinhole collimator and 2 mm diameter of collimated beam was confirmed using a Gafchromic XR-M2 dosimetry film. Scatter volumes were calculated by assuming a cylindrical target geometry with pencil beam radius and scatter thickness as the radius and height of the cylinder respectively (Fig. 6a inset). Transmission corrected photon count and signal-to -noise-ratio (SNR) decreased with decreasing target volume. $AUP_{q=6.3\,nm^{-1}}$ showed almost a linear decrease with scatter thickness ($AUP_{q=6.3\,nm^{-1}} \sim t^{0.94}$, Fig. 6b) until $t = 5$ mm. Similar trend is observed for AUP calculated for $q = 13.1$ nm^{-1} ($AUP_{q=13.1\,nm^{-1}}$, Additional file 1: Figure S8). The scattering profile for $t = 1$ mm was noisier compared to the profiles of $t \geq 5$mm and the corresponding $AUP_{q=6.3\,nm^{-1}}$ shows deviation from the linear scaling.

We further studied the sensitivity of sSAXS to the compaction of oligomer deposits (Fig. 6c, d, Additional file 1: Figure S9 and 10). Loosely bound oligomer deposits showed a shift in peak positions to $q = 7.4$ and 14.5 nm^{-1} with a slightly broader intra β-sheet peak compared to 36% more compact plaque (Fig. 6c and Additional file 1: Figure S10a). The AUP of inter and intra β-sheet peaks showed the dependence on the protein packing density (Fig. 6d). An increase in BSA packing
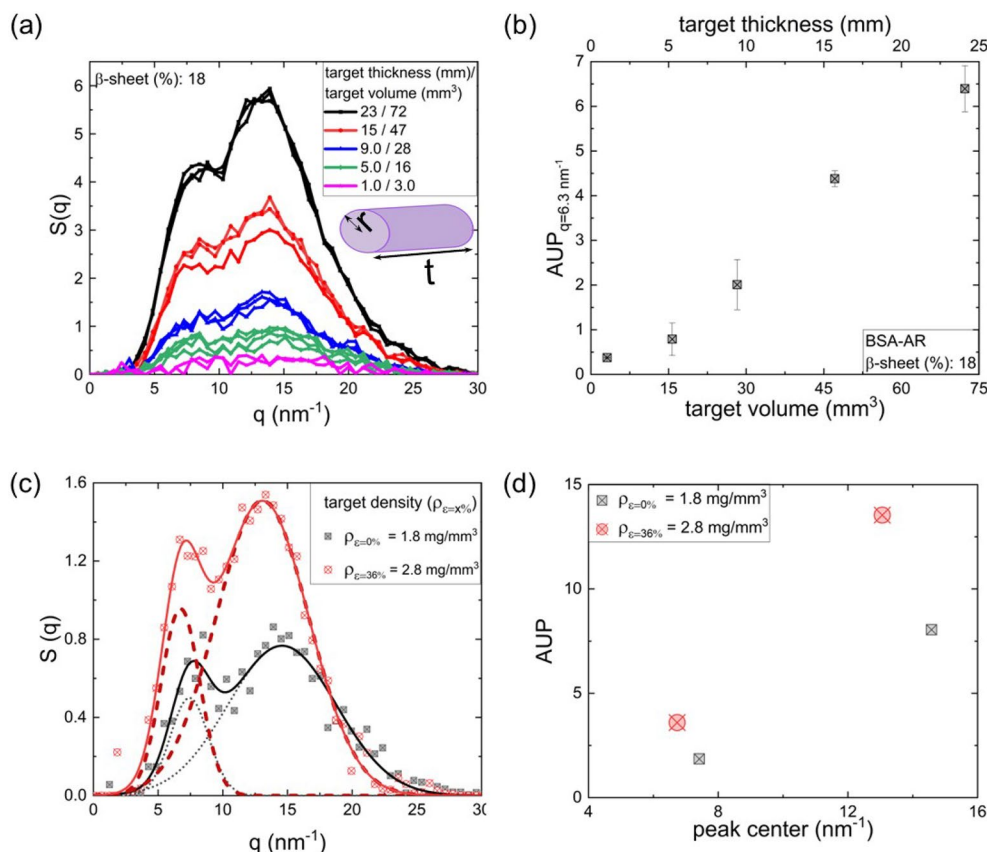

Fig. 6 sSAXS performance at different oligomer volumes and packing densities. **a** sSAXS scattering profiles collected at 80 keV, 1 mA, 300 s X-ray exposure for different BSA oligomer (18% β-sheet) volumes. **b** AUP at $q = 6.3$ nm^{-1} variation with target thickness and volume **c** sSAXS scattering profiles of two different oligomer packing densities; $\rho_{\varepsilon=0\%} = 1.8$- and $\rho_{\varepsilon=36\%} = 2.8$ mg/mm^3. d) Variation of area under the peaks (AUP) of inter and intra β-sheets at two different packing densities ($\rho_{\varepsilon=0\%}$ and $\rho_{\varepsilon=36\%}$)

density from 1.8 to 2.8 mg/mm³, achieved by applying 36% compressive strain ($\varepsilon(\%) = -(\frac{l_2-l_1}{l_1}) \times 100$, where l_2 and l_1 are oligomer deposition heights in the syringe as shown in Additional file 1: Figure S9), almost doubled the $AUP_{q=6.3nm^{-1}}$ ($AUP\rho_{\varepsilon=0\%} = 1.8$ and $AUP\rho_{\varepsilon=36\%} = 3.6$). Neuropathology studies of AD brain tissues have described morphologically distinct diffuse and dense core Aβ plaques [104]. Immunohistochemistry, the gold standard for Aβ plaques detection, often fail to identify diffuse plaques [105]. In this context, the sSAXS sensitivity to amyloid packing density and capability to distinct between diffuse and dense deposits are promising. In future, we plan to extend this approach to understand the performance of sSAXS by matching the oligomer and fibrillar plaque densities present in the human brain at different states of the disease.

Limitations of the study

The current study reports that the oligomer and fibril protein models mimic the secondary structure and nanoscopic X-ray scattering properties of recombinant Aβ-42 fibrils and α-synuclein fibrils. The results were compared with the reported structures of in-vivo protein aggregates of β-Amyloid plaque, α-synuclein, Lewy body, tau tangle, prion and TDP-43 (Table 1). However, the properties of BSA and LGAB model systems beyond these length scales and under other varying conditions in complex in vivo environment are beyond the scope of this work and needs further investigations. The performance evaluation and operating parameter optimizations of sSAXS could also be performed using recombinant oligomer and fibrillar protein aggregates which are commercially available. However, these types of bench testing studies require a large quantity of these expensive recombinant proteins for multiple batch testing and reproducibility studies.

Conclusions

We propose two globular proteins which can mimic the structural characteristics of β-sheets of fibrillar and oligomeric states of Aβ and α-synuclein within the length scales of 0.35–45 nm. Our FTIR study shows that the combined electrostatic and thermal modifications of LGAB and BSA at pH 2 and 90 °C led to protein unfolding followed by fibrillization with the formation of parallel β-sheet secondary structures. From solution SAXS and powder WAXS, we show that the elliptical cylinder cross-section and cross-β structure of these artificial fibrils matches well the recombinant Aβ-42 fibrils and α-synuclein fibrils. SAXS and FTIR studies conclude that the parallel β-sheet characteristics of LGAB fibrils match more closely Aβ-42 fibrils and α-synuclein fibrils compared to BSA fibrils. Unmodified ellipsoids of

LGAB and BSA exhibited antiparallel cross-β structure mimicking Aβ-oligomers. These artificial β-sheets are scalable and inexpensive with easily tunable protein secondary structures and proportions. These model structures may provide important advantages as tractable systems for basic studies evaluating the mechanism of monomer assemblies to various higher order structures during fibrillization and for proof-of-concept studies of structural biomarkers with β-sheets. We used these artificial β-sheet models for evaluating an emerging sSAXS-based method to detect β-sheet rich protein aggregates. Spectral SAXS shows accurate quantification of parallel β-sheets of pure LGAB (average % β-sheet: 54), and BSA (33) fibrils. sSAXS also detected antiparallel cross-β motifs of LGAB (55) and BSA (18) oligomers, a promising technique as this remains challenging for existing neuroimaging modalities to identify oligomers. sSAXS performance evaluation with 18% β-sheet BSA oligomer shows accurate detection of β-sheets from tissue equivalent environment (PMMA) and identification of different target thicknesses. Moreover, sSAXS distinguished different protein packing densities, showing promising for identifying morphologically distinct amyloid depositions. Future work will focus on investigating the detection thresholds of sSAXS under different operational conditions.

Abbreviations

AD	Alzheimer's disease
AFM	Atomic force microscopy
AL	Amyloid light-chain
ALS	Amyotrophic lateral sclerosis
ATR-FTIR	Attenuated total reflection Fourier transform infrared
AUP	Area under the peak
Aβ-42	Amyloid β-42
Aβ	Amyloid β
BSA	Bovine serum albumin
BSA-AR	Bovine serum albumin as received
CdTe	Cadmium telluride
CJD	Creutzfeldt-Jakob disease
CSD	Charge sharing discrimination
CSF	Cerebrospinal fluid
FTD	Frontotemporal dementia
FTLD-TDP	Frontotemporal lobar degeneration with TPD-43
IEP	Isoelectric point
LGAB	β-Lactoglobulin genetic A and B mixture
LGAB-AR	β-Lactoglobulin genetic A and B mixture as received
NDDs	Neurodegenerative diseases
OI	Oligomer index
PD	Parkinson's disease
PET	Positron emission tomography
PMMA	Poly (methyl methacrylate)
PrDs	Prion diseases
PrPs	Prion proteins
SAA	Seed amplification assay
SAXS	Small angle X-ray scattering
SDD	Sample to detector distance
SNR	Signal-to -noise-ratio
sSAXS	Spectral small angle X-ray scattering
SWAXS	Small- and wide-angle X-ray scattering
TDP-43	TAR DNA-binding protein 43

TSE	Transmissible spongiform encephalopathies
TTR	Transthyretin
WAXS	Wide-angle X-ray scattering
XRD	X-ray diffraction
α- Syn	Alpha-synuclein

Supplementary Information

The online version contains supplementary material available at https://doi.org/10.1186/s13578-024-01208-6.

Additional file 1: Figure S1. IR spectra deconvolution protocol. **Figure S2.** Zeta potential of LGAB and BSA as a function of solution pH. **Figure S3.** FTIR spectra of LGAB dissolved in pH2 at different concentrations varying from 0.1- 3 wt.%. **Figure S4.** FTIR spectra of LGAB-pH 2 solutions heated at 90 °C for 12 h and 45 °C for 13 days. **Table S1.** Values of the X-ray mass attenuation coefficients (μ_m, eq. S1) as a function of photon energy for PMMA and brain tissue. **Figure S5.** Photographs of (a) BSA and (b) LGAB oligomers blended with PMMA powder. **Figure S6.** sSAXS spectra of PMMA/BSA (a-c) and PMMA/LGAB (d-f) blends with oligomer/PMMA proportions (a, d) 0.8/0.2 (b, e) 0.6/0.4 (c, f) 0.2/0.8. **Figure S7.** Area under the peak of $q = 13.1 nm^{-1}$ ($AUP_{q=13.1nm^{-1}}$) as a function of oligomer weight fraction ($\phi_{oligomer}$) for BSA and LGAB. **Figure S8.** Variation of area under the peak (AUP) of $q = 13.1 nm^{-1}$ with BSA target thickness and volume. **Figure S9.** Photographs of changing the BSA packing density by varying the compressive strain. **Figure S10.** Variation of BSA oligomer peaks full width half maximum (FWHM) and peak height of inter and intra β-sheet peaks of BSA-AR oligomer.

Author contributions
KS, ED and AB designed and conceptualized the project. KS performed experiments, analyzed data and wrote original draft. ED and AB reviewed and edited the manuscript. All authors read and approved the final manuscript.

Availability of data and materials
All data supporting the conclusions of this article are included within the article and in supporting information provided.

Declarations

Ethical approval and consent to participate
Not applicable.

Consent for publication
Not applicable.

Competing interests
The authors have no positions, patents, or financial interests to declare.

References
1. Gustavsson A, Norton N, Fast T, Frölich L, Georges J, Holzapfel D, et al. Global estimates on the number of persons across the Alzheimer's disease continuum. Alzheimer's & Dementia. 2023;19:658–70. https://doi.org/10.1002/alz.12694.
2. World Alzheimer Report; 2023. https://www.alzint.org/what-we-do/research/world-alzheimer-report/
3. Soto C, Pritzkow S. Protein misfolding, aggregation, and conformational strains in neurodegenerative diseases. Nat Neurosci. 2018;21:1332–40.
4. Gan L, Cookson MR, Petrucelli L, La Spada AR. Converging pathways in neurodegeneration, from genetics to mechanisms. Nat Neurosci. 2018;21:1300–9.
5. LaFerla FM, Green KN, Oddo S. Intracellular amyloid-β in Alzheimer's disease. Nat Rev Neurosci. 2007;8:499–509.
6. Shi Y, Zhang W, Yang Y, Murzin AG, Falcon B, Kotecha A, et al. Structure-based classification of tauopathies. Nature. 2021;598:359–63.
7. Fujiwara H, Hasegawa M, Dohmae N, Kawashima A, Masliah E, Goldberg MS, et al. α-Synuclein is phosphorylated in synucleinopathy lesions. Nat Cell Biol. 2002;4:160–4.
8. Silveira JR, Raymond GJ, Hughson AG, Race RE, Sim VL, Hayes SF, et al. The most infectious prion protein particles. Nature. 2005;437:257–61.
9. Sreedharan J, Blair IP, Tripathi VB, Hu X, Vance C, Rogelj B, et al. TDP-43 mutations in familial and sporadic amyotrophic lateral sclerosis. Science. 2008;319:1668–72. https://doi.org/10.1126/science.1154584.
10. Iadanza MG, Jackson MP, Hewitt EW, Ranson NA, Radford SE. A new era for understanding amyloid structures and disease. Nat Rev Mol Cell Biol. 2018;19:755–73.
11. Bemporad F, Chiti F. Protein misfolded oligomers: experimental approaches, mechanism of formation, and structure-toxicity relationships. Chem Biol. 2012;19:315–27. https://doi.org/10.1016/j.chembiol.2012.02.003.
12. Serpell LC, Berriman J, Jakes R, Goedert M, Crowther RA. Fiber diffraction of synthetic α-synuclein filaments shows amyloid-like cross-β conformation. Proc Natl Acad Sci USA. 2000;97:4897–902. https://doi.org/10.1073/pnas.97.9.4897.
13. Koike H, Iguchi Y, Sahashi K, Katsuno M. Significance of oligomeric and fibrillar species in amyloidosis: insights into pathophysiology and treatment. Molecules. 2021;26:5091.
14. Rajamohamedsait HB, Sigurdsson EM. Histological Staining of amyloid and pre-amyloid peptides and proteins in mouse tissue. Methods Mol Biol. 2012;849:411–24. https://doi.org/10.1007/978-1-61779-551-0_28.
15. Villemagne VL, Doré V, Burnham SC, Masters CL, Rowe CC. Imaging tau and amyloid-β proteinopathies in Alzheimer disease and other conditions. Nat Rev Neurol. 2018;14:225–36.
16. Nabers A, Perna L, Lange J, Mons U, Schartner J, Güldenhaupt J, et al. Amyloid blood biomarker detects Alzheimer's disease. EMBO Mol Med. 2018;10: e8763. https://doi.org/10.15252/emmm.201708763.
17. Simonsen AH, Herukka S-K, Andreasen N, Baldeiras I, Bjerke M, Blennow K, et al. Recommendations for CSF AD biomarkers in the diagnostic evaluation of dementia. Alzheimer's & Dementia. 2017;13:274–84. https://doi.org/10.1016/j.jalz.2016.09.008.
18. Alzghool OM, Dongen G, Giessen E, Schoonmade L, Beaino W. α-Synuclein radiotracer development and in vivo imaging: recent advancements and new perspectives. Mov Disord. 2022;37:936–48. https://doi.org/10.1002/mds.28984.

19. Vaneyck J, Yousif TA, Segers-Nolten I, Blum C, Claessens MMAE. Quantitative seed amplification assay: a proof-of-principle study. J Phys Chem B. 2023;127:1735–43. https://doi.org/10.1021/acs.jpcb.2c08326.

20. Siderowf A, Concha-Marambio L, Lafontant D-E, Farris CM, Ma Y, Urenia PA, et al. Assessment of heterogeneity among participants in the Parkinson's Progression Markers Initiative cohort using α-synuclein seed amplification: a cross-sectional study. The Lancet Neurology. 2023;22:407–17.

21. McKhann GM, Knopman DS, Chertkow H, Hyman BT, Jack CR, Kawas CH, et al. The diagnosis of dementia due to Alzheimer's disease: Recommendations from the National Institute on Aging-Alzheimer's Association workgroups on diagnostic guidelines for Alzheimer's disease. Alzheimer's & Dementia. 2011;7:263–9. https://doi.org/10.1016/j.jalz.2011.03.005.

22. Jack CR Jr, Bennett DA, Blennow K, Carrillo MC, Dunn B, Haeberlein SB, et al. NIA-AA research framework: toward a biological definition of Alzheimer's disease. Alzheimer's & Dementia. 2018;14:535–62. https://doi.org/10.1016/j.jalz.2018.02.018.

23. Harada R, Okamura N, Furumoto S, Yanai K. Imaging protein misfolding in the brain using β-sheet ligands. Front Neurosci. 2018;12:585. https://doi.org/10.3389/fnins.2018.00585/full.

24. Leuzy A, Chiotis K, Lemoine L, Gillberg P-G, Almkvist O, Rodriguez-Vieitez E, et al. Tau PET imaging in neurodegenerative tauopathies—still a challenge. Mol Psychiatry. 2019;24:1112–34.

25. Knight AC, Morrone CD, Varlow C, Yu WH, McQuade P, Vasdev N. Head-to-head comparison of Tau-PET radioligands for imaging TDP-43 in post-mortem ALS brain. Mol Imag Biol. 2023;25:513–27. https://doi.org/10.1007/s11307-022-01779-1.

26. Dahal E, Ghammraoui B, Ye M, Smith JC, Badano A. Label-free X-ray estimation of brain amyloid burden. Sci Rep. 2020;10:20505.

27. Dahal E, Ghammraoui B, Badano A. Feasibility of a label-free X-ray method to estimate brain amyloid load in small animals. J Neurosci Methods. 2020;343: 108822.

28. Ghammraoui B, Badano A. Identification of amyloid plaques in the brain using an x-ray photon-counting strip detector. PLoS ONE. 2020;15: e0228720. https://doi.org/10.1371/journal.pone.0228720.

29. Breedlove S, Crentsil J, Dahal E, Badano A. Small-angle X-ray scattering characterization of a β-amyloid model in phantoms. BMC Res Notes. 2020;13:128. https://doi.org/10.1186/s13104-020-04969-8.

30. Dahal E, Ghammraoui B, Badano A. Characterization of materials embedded in thick objects using spectral small-angle x-ray scattering. J Phys D Appl Phys. 2020;53: 245302. https://doi.org/10.1088/1361-6463/ab8248.

31. Choi M, Dahal E, Badano A. Feasibility of imaging amyloid in the brain using small-angle x-ray scattering. Biomed Phys Eng Express. 2021;7: 015008. https://doi.org/10.1088/2057-1976/ab501c.

32. Ke PC, Zhou R, Serpell LC, Riek R, Knowles TPJ, Lashuel HA, et al. Half a century of amyloids: past, present and future. Chem Soc Rev. 2020;49:5473–509.

33. Olzscha H, Schermann SM, Woerner AC, Pinkert S, Hecht MH, Tartaglia GG, et al. Amyloid-like aggregates sequester numerous metastable proteins with essential cellular functions. Cell. 2011;144:67–78.

34. Goldschmidt L, Teng PK, Riek R, Eisenberg D. Identifying the amylome, proteins capable of forming amyloid-like fibrils. Proc Natl Acad Sci USA. 2010;107:3487–92. https://doi.org/10.1073/pnas.0915166107.

35. Krebs MRH, Devlin GL, Donald AM. Amyloid fibril-like structure underlies the aggregate structure across the pH range for β-lactoglobulin. Biophys J. 2009;96:5013–9.

36. Jones S, Manning J, Kad NM, Radford SE. Amyloid-forming peptides from β2-microglobulin—insights into the mechanism of fibril formation in vitro. J Mol Biol. 2003;325:249–57.

37. Law AJR, Leaver J. Effect of pH on the thermal denaturation of whey proteins in milk. J Agric Food Chem. 2000;48:672–9. https://doi.org/10.1021/jf981302b.

38. Lu X, Wintrode PL, Surewicz WK. β-Sheet core of human prion protein amyloid fibrils as determined by hydrogen/deuterium exchange. Proc Natl Acad Sci. 2007;104:1510–5. https://doi.org/10.1073/pnas.0608047104.

39. Choo LP, Wetzel DL, Halliday WC, Jackson M, LeVine SM, Mantsch HH. In situ characterization of beta-amyloid in Alzheimer's diseased tissue by synchrotron Fourier transform infrared microspectroscopy. Biophys J. 1996;71:1672–9.

40. Röhr D, Boon BDC, Schuler M, Kremer K, Hoozemans JJM, Bouwman FH, et al. Label-free vibrational imaging of different Aβ plaque types in Alzheimer's disease reveals sequential events in plaque development. Acta Neuropathol Commun. 2020;8:222. https://doi.org/10.1186/s40478-020-01091-5.

41. Araki K, Yagi N, Ikemoto Y, Yagi H, Choong C-J, Hayakawa H, et al. Synchrotron FTIR micro-spectroscopy for structural analysis of Lewy bodies in the brain of Parkinson's disease patients. Sci Rep. 2015;5:17625.

42. Banerjee S, Ghosh A. Structurally distinct polymorphs of tau aggregates revealed by nanoscale infrared spectroscopy. J Phys Chem Lett. 2021;12:11035–41. https://doi.org/10.1021/acs.jpclett.1c02660.

43. Al-Hilaly YK, Hurt C, Rickard JE, Harrington CR, Storey JMD, Wischik CM, et al. Solid-state NMR of paired helical filaments formed by the core tau fragment tau(297–391). Front Neurosci. 2022;16: 988074. https://doi.org/10.3389/fnins.2022.988074/full.

44. Ostapchenko VG, Sawaya MR, Makarava N, Savtchenko R, Nilsson KPR, Eisenberg D, et al. Two amyloid states of the prion protein display significantly different folding patterns. J Mol Biol. 2010;400:908–21.

45. Zhu L, Xu M, Yang M, Yang Y, Li Y, Deng J, et al. An ALS-mutant TDP-43 neurotoxic peptide adopts an anti-parallel β-structure and induces TDP-43 redistribution. Hum Mol Genet. 2014;23:6863–77. https://doi.org/10.1093/hmg/ddu409.

46. Michael R, Lenferink A, Vrensen GFJM, Gelpi E, Barraquer RI, Otto C. Hyperspectral Raman imaging of neuritic plaques and neurofibrillary tangles in brain tissue from Alzheimer's disease patients. Sci Rep. 2017;7:15603.

47. Zandomeneghi G, Krebs MRH, McCammon MG, Fändrich M. FTIR reveals structural differences between native β-sheet proteins and amyloid fibrils. Protein Sci. 2009;13:3314–21. https://doi.org/10.1110/ps.041024904.

48. Berriman J, Serpell LC, Oberg KA, Fink AL, Goedert M, Crowther RA. Tau filaments from human brain and from in vitro assembly of recombinant protein show cross-β structure. Proc Natl Acad Sci USA. 2003;100:9034–8. https://doi.org/10.1073/pnas.1530287100.

49. Pan KM, Baldwin M, Nguyen J, Gasset M, Serban A, Groth D, et al. Conversion of alpha-helices into beta-sheets features in the formation of the scrapie prion proteins. Proc Natl Acad Sci. 1993;90:10962–6. https://doi.org/10.1073/pnas.90.23.10962.

50. Groveman BR, Dolan MA, Taubner LM, Kraus A, Wickner RB, Caughey B. Parallel in-register intermolecular β-sheet architectures for prion-seeded prion protein (PrP) amyloids. J Biol Chem. 2014;289:24129–42.

51. Shenoy J, El Mammeri N, Dutour A, Berbon M, Saad A, Lends A, et al. Structural dissection of amyloid aggregates of TDP-43 and its C-terminal fragments TDP-35 and TDP-16. FEBS J. 2020;287:2449–67. https://doi.org/10.1111/febs.15159.

52. Kirschner DA, Abraham C, Selkoe DJ. X-ray diffraction from intraneuronal paired helical filaments and extraneuronal amyloid fibers in Alzheimer disease indicates cross-beta conformation. Proc Natl Acad Sci USA. 1986;83:2776–2776. https://doi.org/10.1073/pnas.83.8.2776-b.

53. Araki K, Yagi N, Aoyama K, Choong C-J, Hayakawa H, Fujimura H, et al. Parkinson's disease is a type of amyloidosis featuring accumulation of amyloid fibrils of α-synuclein. Proc Natl Acad Sci USA. 2019;116:17963–9. https://doi.org/10.1073/pnas.1906124116.

54. Horwich AL, Weissman JS. Deadly Conformations—Protein Misfolding in Prion Disease. Cell. 1997;89:499–510.

55. Wille H, Bian W, McDonald M, Kendall A, Colby DW, Bloch L, et al. Natural and synthetic prion structure from X-ray fiber diffraction. Proc Natl Acad Sci USA. 2009;106:16990–5. https://doi.org/10.1073/pnas.0909006106.

56. Zhuo X-F, Wang J, Zhang J, Jiang L-L, Hu H-Y, Lu J-X. Solid-State NMR reveals the structural transformation of the TDP-43 amyloidogenic region upon fibrillation. J Am Chem Soc. 2020;142:3412–21. https://doi.org/10.1021/jacs.9b10736.

57. Kumar ST, Nazarov S, Porta S, Maharjan N, Cendrowska U, Kabani M, et al. Seeding the aggregation of TDP-43 requires post-fibrillization proteolytic cleavage. Nat Neurosci. 2023;26:983–96.

58. Li D, Liu C. Conformational strains of pathogenic amyloid proteins in neurodegenerative diseases. Nat Rev Neurosci. 2022;23:523–34.

Suresh *et al. Cell & Bioscience*   (2024) 14:26

Page 17 of 18

59. Yang Y, Arseni D, Zhang W, Huang M, Lövestam S, Schweighauser M, et al. Cryo-EM structures of amyloid-β 42 filaments from human brains. Science. 2022;375:167–72. https://doi.org/10.1126/science.abm7285.

60. Xue W-F, Homans SW, Radford SE. Amyloid fibril length distribution quantified by atomic force microscopy single-particle image analysis. Protein Eng Des Sel. 2009;22:489–96. https://doi.org/10.1093/protein/gzp026.

61. Li B, Ge P, Murray KA, Sheth P, Zhang M, Nair G, et al. Cryo-EM of full-length α-synuclein reveals fibril polymorphs with a common structural kernel. Nat Commun. 2018;9:3609.

62. Grazia Spillantini M, Anthony Crowther R, Jakes R, Cairns NJ, Lantos PL, Goedert M. Filamentous α-synuclein inclusions link multiple system atrophy with Parkinson's disease and dementia with Lewy bodies. Neurosci Lett. 1998;251:205–8.

63. Guerrero-Ferreira R, Taylor NM, Arteni A-A, Kumari P, Mona D, Ringler P, et al. Two new polymorphic structures of human full-length alpha-synuclein fibrils solved by cryo-electron microscopy. Elife. 2019;8: e48907.

64. Glynn C, Sawaya MR, Ge P, Gallagher-Jones M, Short CW, Bowman R, et al. Cryo-EM structure of a human prion fibril with a hydrophobic, protease-resistant core. Nat Struct Mol Biol. 2020;27:417–23.

65. Kraus A, Hoyt F, Schwartz CL, Hansen B, Artikis E, Hughson AG, et al. High-resolution structure and strain comparison of infectious mammalian prions. Mol Cell. 2021;81:4540-4551.e6.

66. Chu BKY, Tsai R, Hung C, Kuo Y, Chen EHL, Chiang Y, et al. Location of the cross-β structure in prion fibrils: a search by seeding and electron spin resonance spectroscopy. Protein Sci. 2022. https://doi.org/10.1002/pro.4326.

67. Wang L-Q, Zhao K, Yuan H-Y, Wang Q, Guan Z, Tao J, et al. Cryo-EM structure of an amyloid fibril formed by full-length human prion protein. Nat Struct Mol Biol. 2020;27:598–602.

68. Mompeán M, Hervás R, Xu Y, Tran TH, Guarnaccia C, Buratti E, et al. Structural evidence of amyloid fibril formation in the putative aggregation domain of TDP-43. J Phys Chem Lett. 2015;6:2608–15. https://doi.org/10.1021/acs.jpclett.5b00918.

69. Arseni D, Hasegawa M, Murzin AG, Kametani F, Arai M, Yoshida M, et al. Structure of pathological TDP-43 filaments from ALS with FTLD. Nature. 2022;601:139–43.

70. Shimonaka S, Nonaka T, Suzuki G, Hisanaga S, Hasegawa M. Templated aggregation of TAR DNA-binding protein of 43 kDa (TDP-43) by seeding with TDP-43 peptide fibrils. J Biol Chem. 2016;291:8896–907.

71. Sarroukh R, Goormaghtigh E, Ruysschaert JM, Raussens V. ATR-FTIR: A "rejuvenated" tool to investigate amyloid proteins. Biochimica et Biophysica Acta BBA - Biomembranes. 2013;1828:2328–38.

72. Barth A. Infrared spectroscopy of proteins. Biochimica et Biophysica Acta BBA - Bioenergetics. 2007;1767:1073–101.

73. Carbonaro M, Nucara A. Secondary structure of food proteins by Fourier transform spectroscopy in the mid-infrared region. Amino Acids. 2010;38:679–90. https://doi.org/10.1007/s00726-009-0274-3.

74. Tatulian SA. Structural characterization of membrane proteins and peptides by FTIR and ATR-FTIR spectroscopy. In: Kleinschmidt JH, editor. Lipid-protein interactions. Totowa: Humana Press; 2013. p. 177–218. https://doi.org/10.1007/978-1-62703-275-9_9.

75. Lake JA. An iterative method of slit-correcting small angle X-ray data. Acta Crystallogr A. 1967;23:191–4.

76. Jowitt L, Wilson M, Seller P, Angelsen C, Wheater RM, Cline B, et al. HEXITEC 2 × 2 tiled hard X-ray spectroscopic imaging detector system. J Instrum. 2022;17:P01012. https://doi.org/10.1088/1748-0221/17/01/P01012.

77. Sarroukh R, Cerf E, Derclaye S, Dufrêne YF, Goormaghtigh E, Ruysschaert J-M, et al. Transformation of amyloid β(1–40) oligomers into fibrils is characterized by a major change in secondary structure. Cell Mol Life Sci. 2011;68:1429–38. https://doi.org/10.1007/s00018-010-0529-x.

78. Chirgadze YN, Nevskaya NA. Infrared spectra and resonance interaction of amide-I vibration of the antiparallel-chain pleated sheet. Biopolymers. 1976;15:607–25. https://doi.org/10.1002/bip.1976.360150402.

79. Cerf E, Sarroukh R, Tamamizu-Kato S, Breydo L, Derclaye S, Dufrêne YF, et al. Antiparallel β-sheet: a signature structure of the oligomeric amyloid β-peptide. Biochem J. 2009;421:415–23.

80. Murakami K, Irie K, Morimoto A, Ohigashi H, Shindo M, Nagao M, et al. Neurotoxicity and physicochemical properties of Aβ mutant peptides from cerebral amyloid angiopathy. J Biol Chem. 2003;278:46179–87.

81. Lin S-Y, Chu H-L, Wei Y-S. Secondary conformations and temperature effect on structural transformation of amyloid β(1–28), (1–40) and (1–42) peptides. J Biomol Struct Dyn. 2003;20:595–601. https://doi.org/10.1080/07391102.2003.10506876.

82. Bouchard M, Zurdo J, Nettleton EJ, Dobson CM, Robinson CV. Formation of insulin amyloid fibrils followed by FTIR simultaneously with CD and electron microscopy. Protein Sci. 2000;9:1960–7. https://doi.org/10.1110/ps.9.10.1960.

83. Zhang H, Kaneko K, Nguyen JT, Livshits TL, Baldwin MA, Cohen FE, et al. Conformational transformations in peptides containing two putative α-helices of the prion protein. J Mol Biol. 1995;250:514–26.

84. Bukackova M, Rusnok P, Marsalek R. Mathematical methods in the calculation of the zeta potential of BSA. J Solution Chem. 2018;47:1942–52. https://doi.org/10.1007/s10953-018-0830-0.

85. Taulier N, Chalikian TV. Characterization of pH-induced transitions of β-lactoglobulin: ultrasonic, densimetric, and spectroscopic studies 1. J Mol Biol. 2001;314:873–89.

86. van den Akker CC, Engel MFM, Velikov KP, Bonn M, Koenderink GH. Morphology and persistence length of amyloid fibrils are correlated to peptide molecular structure. J Am Chem Soc. 2011;133:18030–3. https://doi.org/10.1021/ja206513r.

87. Ikeda S, Nishinari K. Structural changes during heat-induced gelation of globular protein dispersions. Biopolymers. 2001;59:87–102. https://doi.org/10.1002/1097-0282(200108)59:2%3c87::AID-BIP1008%3e3.0.CO;2-H.

88. Nandi I, Chall S, Chowdhury S, Mitra T, Roy SS, Chattopadhyay K. Protein fibril-templated biomimetic synthesis of highly fluorescent gold nanoclusters and their applications in cysteine sensing. ACS Omega. 2018;3:7703–14. https://doi.org/10.1021/acsomega.8b01033.

89. Yoneyama H, Yamashita M, Kasai S, Kawase K, Ueno R, Ito H, et al. Terahertz spectroscopy of native-conformation and thermally denatured bovine serum albumin (BSA). Phys Med Biol. 2008;53:3543–9. https://doi.org/10.1088/0031-9155/53/13/010.

90. Lattanzi V, André I, Gasser U, Dubackic M, Olsson U, Linse S. Amyloid β 42 fibril structure based on small-angle scattering. Proc Natl Acad Sci. 2021. https://doi.org/10.1073/pnas.2112783118.

91. Festa G, Mallamace F, Sancesario GM, Corsaro C, Mallamace D, Fazio E, et al. Aggregation states of Aβ1–40, Aβ1–42 and Aβp3–42 amyloid beta peptides: a SANS study. Int J Mol Sci. 2019;20:4126.

92. Yong W, Lomakin A, Kirkitadze MD, Teplow DB, Chen S-H, Benedek GB. Structure determination of micelle-like intermediates in amyloid β-protein fibril assembly by using small angle neutron scattering. Proc Natl Acad Sci. 2002;99:150–4. https://doi.org/10.1073/pnas.012584899.

93. Quillin ML, Matthews BW. Accurate calculation of the density of proteins. Acta Crystallogr D Biol Crystallogr. 2000;56:791–4.

94. Pogostin BH, Linse S, Olsson U. Fibril charge affects α-synuclein hydrogel rheological properties. Langmuir. 2019;35:16536–44. https://doi.org/10.1021/acs.langmuir.9b02516.

95. Svergun DI, Koch MHJ. Small-angle scattering studies of biological macromolecules in solution. Rep Prog Phys. 2003;66:1735–82. https://doi.org/10.1088/0034-4885/66/10/R05.

96. Shannon CE. A mathematical theory of communication. Bell Syst Tech J. 1948;27:379–423.

97. Sawaya MR, Sambashivan S, Nelson R, Ivanova MI, Sievers SA, Apostol MI, et al. Atomic structures of amyloid cross-β spines reveal varied steric zippers. Nature. 2007;447:453–7.

98. Stroud JC, Liu C, Teng PK, Eisenberg D. Toxic fibrillar oligomers of amyloid-β have cross-β structure. Proc Natl Acad Sci. 2012;109:7717–22. https://doi.org/10.1073/pnas.1203193109.

99. Gu L, Liu C, Stroud JC, Ngo S, Jiang L, Guo Z. Antiparallel triple-strand architecture for prefibrillar Aβ42 oligomers. J Biol Chem. 2014;289:27300–13.

100. Suresh K, Sharma DK, Chulliyil R, Sarode KD, Kumar VR, Chowdhury A, et al. Single-particle tracking to probe the local environment in ice-templated crosslinked colloidal assemblies. Langmuir. 2018;34:4603–13. https://doi.org/10.1021/acs.langmuir.7b04120.

Suresh *et al. Cell & Bioscience*   (2024) 14:26

Page 18 of 18

101. Araki K, Yagi N, Nakatani R, Sekiguchi H, So M, Yagi H, et al. A small-angle X-ray scattering study of alpha-synuclein from human red blood cells. Sci Rep. 2016;6:30473.
102. Hamideen MS, Abady RS, Sharaf JM. Study on mass and linear attenuation coefficients of PMMA as human tissue-equivalent material. Latv J Phys Tech Sci. 2022;59:64–73. https://doi.org/10.2478/lpts-2022-0012.
103. Tartari A, Casnati E, Bonifazzi C, Baraldi C. Molecular differential cross sections for x-ray coherent scattering in fat and polymethyl meth-acrylate. Phys Med Biol. 1997;42:2551–60. https://doi.org/10.1088/0031-9155/42/12/018.
104. Dickson TC, Vickers JC. The morphological phenotype of β-amyloid plaques and associated neuritic changes in Alzheimer's disease. Neuro-science. 2001;105:99–107.
105. Ikonomovic MD, Buckley CJ, Abrahamson EE, Kofler JK, Mathis CA, Klunk WE, et al. Post-mortem analyses of PiB and flutemetamol in diffuse and cored amyloid-β plaques in Alzheimer's disease. Acta Neuropathol. 2020;140:463–76. https://doi.org/10.1007/s00401-020-02175-1.

Publisher's Note